Larrañaga-Valsero, B., Smith, R. A., Tayong, R. B., Fernández-López, A., & Güemes, A. (2018). Wrinkle measurement in glass-carbon hybrid laminates comparing ultrasonic techniques: A case study. *Composites Part A: Applied Science and Manufacturing*, *114*, 225-240. https://doi.org/10.1016/j.compositesa.2018.08.014

Wrinkle measurement in glass-carbon hybrid laminates comparing ultrasonic techniques: A case Study.

Beatriz Larrañaga-Valsero[1], Robert A. Smith[2],
Rostand B. Tayong[2], Antonio Fernández-López[1] and Alfredo Güemes[1].

[1]Department of Materials and Aerospace Production. Polytechnic University of Madrid, SPAIN.

[2] Department of Mechanical Engineering, University of Bristol, BS8 1TR, UK

Abstract

Wrinkles, (also known as out-of-plane waviness) are, unfortunately, a common phenomenon that has caused some wind-turbine blades to unexpectedly fail in service. Being able to detect the wrinkles while in the factory will reduce the risk of catastrophic failure and characterising the wrinkles would minimise the repaired area, thus increasing the efficiency of the repair and the design. This work compares the effectiveness of three different ultrasound techniques for detecting and characterising out-of-plane wrinkles in the typical glass-carbon hybrid laminates that are used for wind-turbine blades. The tests samples were manufactured so that the laminates and the defects are representative of those used in the wind-turbine industry. Basic mechanical tests were performed to check the drop in mechanical properties due to wrinkling. The ideal probe frequency was determined as the resonance frequency of the plies using an analytical ultrasonic-propagation model. The three different ultrasound techniques used are: full-matrix capture (FMC) with the total focusing method (TFM), a commercial phased-array instrument and an immersion test with a raster-scanned single-element focused probe. When possible, severity parameters of the wrinkle were measured on the ultrasonic images and compared with the measurements of the actual sample in order to determine which method best characterises such wrinkles and which would be more appropriate to implement in an industrial environment. Not all of the techniques allowed full characterisation of out-of-plane waviness on the specimens. The FMC/TFM method gave better results whilst phased-array technology and single-element immersion testing presented more challenges. An additional enhancement to the TFM imaging was achieved using an Adapted-TFM method with an angle-dependent velocity correction.

Keywords: A. Carbon Fibre; A. Glass Fibre; D. Non-destructive testing

1. Introduction

The development and utilization of wind power for energy generation has increased worldwide since the energy crisis in 1970 mainly because it is now a mature green technology. Nowadays, giant wind turbines are being developed[(1)] with enormous turbine blades that are designed using thick carbon- and glass-fibre laminates in order to withstand the large bending moments that appear at the root of those parts. Unfortunately, during the manufacturing process of such laminates, misalignment in fibre orientation is a common defect that seriously degrades the mechanical properties [(2)]. When such defects are not detected during the manufacturing process, the blades may unexpectedly fail in service, which forces wind-farm operators to repair the blades in-situ if the failure has not destroyed the whole turbine. These kinds of repairs are expensive and inconvenient [(3)]. In order to reduce the risk of catastrophic failure, the

designers over-engineer by adding even more plies, and weight, to the blades. If fibre or ply misalignment were detectable during the manufacturing process, the blades could be repaired before leaving the factory, which would avoid expensive in-situ repairs and would allow the designers to refine the laminates. Hence, it is important that the increasingly large parts manufactured by the industry are fully characterised.

Misalignments in fibre orientation (out-of-plane and in-plane waviness) are inherent to the manufacturing process generally chosen for making turbine blades. The formation of wrinkles (out-of-plane waviness) during the manufacture of the blades is a complex process that results from local buckling, lamination residual stresses, an incorrect curing procedure, unintended foreign bodies or inserts, etc. [(4)]. Due to the manufacturing process and the dimensions of the blades, the wrinkles that appear in these thick laminates have a specific geometry. In the literature, several parameters have been used to characterise the misalignment with respect to loading direction (Figure 1): maximum amplitude (H) [(5)], severity [(6)] or maximum angle [(7)]. The geometry of wrinkles found in case-study blades and the parameters chosen are shown in Figure 1. L is defined as a wrinkle wavelength so the 'severity' of the wrinkle (A/L) is consistent with the literature[(8)].

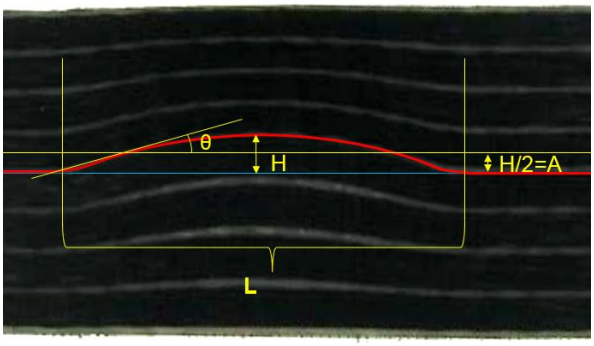

Figure 1: Wrinkle parameters

In order to detect any defect that may have appeared during the manufacturing process before the blades are installed in the wind farms, several non-destructive testing techniques are already in use[(9)] although not every technique allows the detection of wrinkles. Even though Micro-focus X-Ray Computed Tomography (Micro-CT) is the technique that provides the most detailed information for 3D characterisation of fibre orientation on small components; it is expensive and it is not a practical technique for large components[(10-11)] due to the trade-off between resolution and component size. In components as large as turbine blades Micro-CT does not achieve sufficient resolution of ply boundaries (requires 20 µm voxel size or less) and, therefore, wrinkles, so other techniques must be considered. For CFRP blades, eddy-current imaging enables detection of some kinds of surface and subsurface damage [(12)]. Some experiments have been done with cross-ply laminates trying to detect surface waviness and subsurface in-plane waviness using a rectangular race-track coil[(13-14)]. The results showed that this technique can detect and characterise the size and shape of surface waviness with adequate accuracy whereas it significantly underestimated the size of the subsurface waviness. In addition, this eddy-current imaging method does not work on GFRP blades nor can it detect in-plane waviness when the direction of the carbon fibre plies with waviness is perpendicular to the long sides of the rectangular driver coil. For CFRP samples, circular probes would be required to use the electrical anisotropy of the material and avoid this limitation[(12)]. For the glass-carbon hybrid laminates commonly used on turbine blades, eddy-current imaging is not a suitable technique for detecting

sub-surface wrinkles. Ultrasonic techniques are commonly used for composite-material inspection. This technique provides an easy detection of delamination and porosity embedded in the laminate because those kinds of defects provoke either a high reflection or high attenuation of normal-incidence ultrasonic signals, respectively. Ultrasonic techniques providing an acceptable detail level for 3D characterisation of fibre orientation can be used on large components and allow the inspection of both glass and carbon fibre. The ply lay-up of composite materials can be imaged through the 3D ultrasonic full-waveform scans of the samples[15-17]. However, unlike Micro-CT, the raw datasets from an ultrasonic inspection do not automatically reveal the ply lay-up using the common 'gate' method of signal analysis. Current research shows how the depths of the resin layers can be tracked using the instantaneous amplitude, phase and frequency of the ultrasonic response in 3D scans, allowing out-of-plane wrinkles to be mapped within the structure [18-19]. These instantaneous parameters are defined via the following equation for the analytic signal[17]:

$$x_a(t) = A(t)e^{i\phi(t)} \qquad (1)$$

where $A(t)$ is the instantaneous amplitude and $\phi(t)$ is the instantaneous phase at time t. The imaginary part of the analytic signal is calculated by applying a Hilbert transform to the measured (real) waveform[20]. The instantaneous frequency, $f(t)$ is the rate of change of phase at time t in the response at the measurement location and is given[21] by:

$$f(t) = \frac{1}{2\pi}\frac{d\phi}{dt}. \qquad (2)$$

The instantaneous amplitude, $A(t)$, is the magnitude, or envelope, of the signal.

In the present work, three samples with out-of-plane wrinkles in thick carbon/glass laminates, similar to those that appear at the root of turbine blades, were manufactured and are described in Section 2. The coupons were mechanically tested to determine the real detriment in mechanical properties that such wrinkles can cause and results are given in Section 3. The ultrasonic testing is modelled in Section 4 and, in Section 5, three different ultrasonic data-acquisition techniques are compared - full-matrix capture (FMC) with total-focusing method (TFM) reconstruction, phased-array ultrasound and an immersion test with a raster-scanned single-element probe. Finally, in Section 6, a new adapted-TFM method, which corrects for anisotropic material properties using an angle-dependent velocity, is compared with the other methods and with the modelled results.

2. Sample-manufacturing Procedure

A total of five thick composite samples were made. The lay-ups, defect shapes and sizes were chosen based on lay-ups, defect shapes and sizes observed in the manufacture of real turbine blades. Two prepreg materials were used for the manufacture of the parts: epoxy resin reinforced with either unidirectional carbon fibre with a nominal ply thickness of 0.6 mm and fibres in the 0° or load direction; or woven +/- 45 glass fibre with a nominal woven-ply thickness of 0.44 mm. Two different lay-ups are used for the experiments: 1) one woven glass ply every six plies (one glass ply followed by five carbon plies) (Specimens B and C and Pristine 1) and 2) all carbon fibre except the first and last plies, which were of woven glass fibre (Specimen D and Pristine 2). All the carbon plies had fibres in the same direction – the load direction. Two test samples named Pristine 1 and Pristine 2, one for each lay-up, were manufactured with flat plies and without defects and are considered the ‘pristine’ references for the mechanical tests. Three test samples named B, C and D (see Figure 2: Samples B (left), C (middle) and D

(right)Figure 2: Samples B (left), C (middle) and D (right).) were made in a two-step process with internal wrinkles.

Figure 2: Samples B (left), C (middle) and D (right). Images not scaled equally.

All the samples were measured for total thickness, wrinkle maximum height, H, "severity", A/L and wrinkle angle, θ. The wrinkle angle was measured from the slope of the tangent to the curve at the point where it intersects with the imaginary in-plane line at a distance A from the flat part of the wrinkle – see Figure 1. A summary of the values measured for the panels are given in Table 1 and should be interpreted with reference to Figure 1. The nominal fibre volume fraction was not measured but 60% is considered for the non-wrinkles areas because images indicate good ply consolidation. Nominal inter-ply resin-layer thickness is considered to be 0.01 mm in the ultrasonic model.

Table 1: Characteristics of the Test Specimens

Specimen	Pristine 1	B	C	Pristine 2	D
Lay-up	1 x glass woven, 5 x carbon UD			Carbon UD except front & back in woven glass	
Thickness	25 mm	27 mm	26 mm	22 mm	23 mm
Number of Plies	49	49	49	42	42
Wrinkle Maximum height H	0 mm	3 mm	6 mm	0 mm	3 mm
Wrinkle “Severity” A/L	0	0.030	0.090	0	0.030
Wrinkle Angle θ	0º	8.5º	24º	0º	8.5º

The samples with internal wrinkles were designed to have a wrinkle of cosine geometry in the middle. Firstly two aluminium male tools were manufactured with the chosen protruding cosine wrinkle geometry so that the samples would have a middle ply with a known maximum wrinkle amplitude. For each sample, half of the plies were manually stacked such that fibres follow the defect profile, and cured in a hot plate press. During this process the consolidation of the plies over the defect was not perfect and the severity of the wrinkle obtained in the cured part was not as great as the severity of the cosine geometry of the tool, causing a deviation from the intended shape (see Figure 3). This was caused by the stiffness of the carbon and glass fibres that made it difficult to get the pre-preg to adapt to the tool shape. Then, the aluminium tool was removed and the remaining layers were manually stacked using the cured half laminate as a tool. The intended top flat geometry is assured by the hot plate press. Figure 3 shows a diagram of the two steps of the manufacturing process. Again, it was difficult to force the pre-preg into the concave geometry and specimen C (the specimen with the most severe wrinkle) has a thick resin-rich layer with voids caused by the resistance of the fibres to bend – sometimes called a ‘bridging’ defect. The number of plies of each sample assures that the wrinkle affects the full width of the parts.

The lateral dimensions of the manufactured panels were 300mm x 300mm. Mechanical testing samples were cut from half of the panel, orthogonal to the wrinkles and parallel

to the 0° direction, such that carbon fibers ran along the loading axis. The remaining part of the panel was used for the ultrasonic experiments.

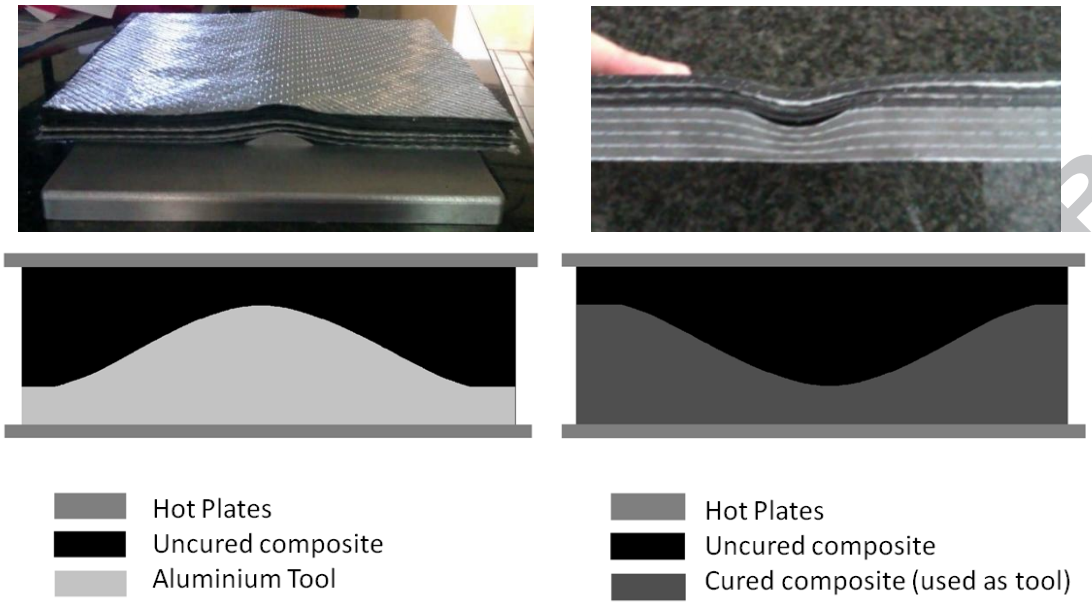

Figure 3: Diagram of the two steps of the manufacturing process (first step on the left, second step on the right). Aluminium tool used during the manufacture of the specimens with half of the plies stacked on it before curing (Top left). The effect where the layers do not conform to the geometry of the tool can be seen clearly (Top).

3. Mechanical testing

In order to determine the degradation that these particular wrinkles had caused in the mechanical properties of the material, comprehensive tensile and compression tests were carried out. Ten coupons (five compression coupons, five tensile coupons) were tested for each sample. Tests were conducted at room temperature 24 ºC and average humidity of 55% under atmospheric pressure.

For the tensile properties the UNE-EN ISO 527[(22)] standard test conditions for unidirectional composite reinforced plastics have been followed. The tests of the pristine samples were conducted according to respective standards using a testing machine MTS 810 equipped with a 100 k-N load cell and a 25 mm extensometer. The coupons of samples B, C, and D were cut with the same dimensions as the coupons of the pristine samples so that the results are comparable. The dimensions of the coupons were 250 mm long and 4 mm width, except for the pristine specimens without induced wrinkling, whose nominal width was reduced by half (2 mm) following the recommendations given by UNE-EN ISO 527, due to the high required loads. The other dimension of the cross section was given by the thickness of the laminate, given at Table 1. The width was adjusted with a machining process. Tests were conducted at a crosshead displacement speed of 2 ± 0.5 mm / min.

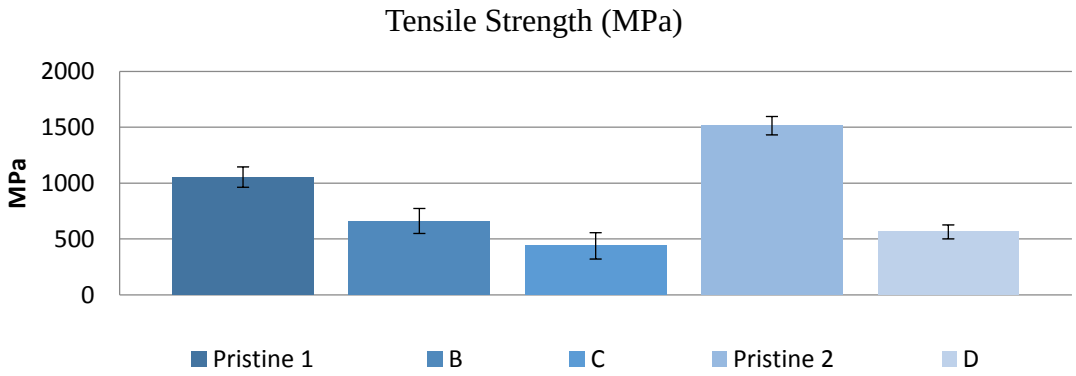

Figure 4: Tensile Strength (MPa) of samples Pristine 1, B, C, Pristine 2, and D.

Figure 4 shows a comparative study between the five samples. As can be observed the presence of the wrinkle in the laminates degrades severely the tensile properties. The presence of the internal woven glass-layers in Pristine 1, which is the only difference between Pristine 1 and Pristine 2, degraded the tensile strength by up to 30%. The woven glass layers are added in order to reduce the manufacturing costs but the blades thus manufactured meet all the mechanical requirements of the structure. The tensile strengths of specimens B and C were respectively 37% and 58% of the tensile strength of Pristine 1. The tensile strength was approximately 63% lower in specimen D than in Pristine 2.

For the compression properties, the ASTM D695[23] modified version of ISO 14126: 1999[24], was followed. This method was chosen from among the many different methods for composite material because of the configuration of the specimens. Also, the modification of the tool was done in such a way that the compression load is transmitted to the material by direct load on one of the ends, thus fulfilling the condition that the final break of the specimen takes place with a flexural deformation below 10%. The tests of the pristine samples were conducted according to respective standards using a testing machine (INSTRON 4202) equipped with a 100 k-N load cell. The coupons of samples B, C, and D were cut with the same dimensions as the coupons of the pristine samples so that the results are comparable. The required dimensions of the specimens were 80 mm in length and 4 mm in width. The thickness of the specimen is conditioned by the thickness of the laminate. Tests were conducted at a crosshead displacement speed of 1 +/- 0.5 mm / min.

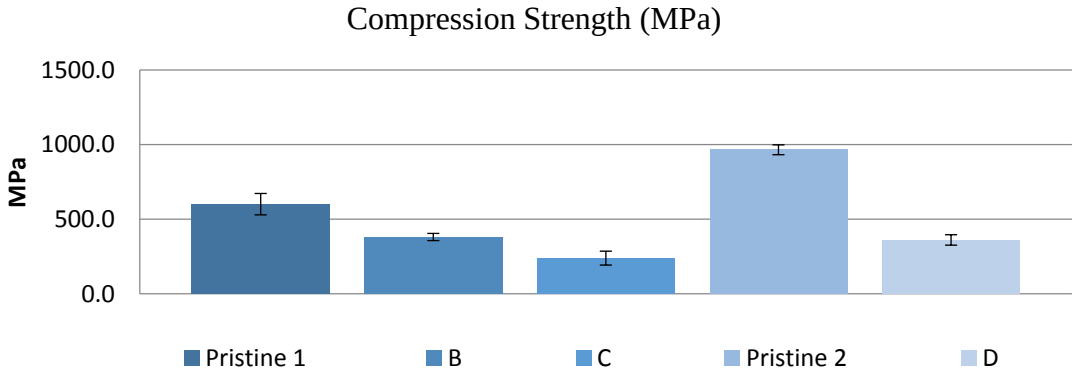

Figure 5: Compression Strength (MPa) of samples Pristine 1, B, C Pristine 2 and D.

Figure 5 shows a comparative study between the five samples. It should be noted that the presence of the internal woven-glass layers again adversely affect the mechanical properties (causing a 38% decrease in compression strength). The compression strengths of specimens B and C were respectively 37% and 60% of the compression strength of Pristine 1. The compression strength was approximately 63% lower in specimen D than in Pristine 2. Thus the wrinkle has approximately the same influence on the compression properties as the tensile properties.

4. Ultrasonic analytical modelling

In order to visualize the wrinkles with an ultrasonic inspection, it is necessary to enhance the reflections from the thin resin layer located in-between plies in the composite stack. This is achieved close to the resonance frequency of the plies. This is why the ply resonance frequency determines the ideal probe frequency and bandwidth of the ultrasonic inspections[25]. Smith[26] has developed a one-dimensional normal-incidence analytical model that can be used to simulate the response of a composite laminate for a normal-incidence plane wave based on the thickness, density and compression modulus of each layer. In this one-dimensional model, wrinkles can be modelled by gradually changing the layer properties.

This is a recursive frequency-domain model that calculates the pulse-echo frequency response of the laminate and convolves it with the frequency-domain input signal. If a water stand-off is used, the frequency-dependent attenuation in the water is not accounted for because the input pulse is assumed to be defined at the front surface. Effective-medium properties are calculated for each composite layer using Hashin mixture rules[27,28]. The specimens are modelled in immersion (with both upper and lower surfaces of the laminate connected to water). The compression modulus and density figures for the resin, carbon and glass fibres that are built into the model are as follows in Table 2.

Table 2: Material properties of component materials used with the Hashin[27,28] mixture rules.

	Compression Modulus, M_{11} (GPa)	Density (kg/m^3)	Attenuation Coefficient (dB/mm/MHz)	Poisson Ratio
Water	2.05	998	n/a (see text)	0.5
Epoxy resin	10.7	1270	0.15	0.37
Carbon Fibre	16.0	1690	0	0.28
E-glass	80.2	2570	0	0.20

The model had been coded in Matlab and initially 18-ply non-wrinkled laminates were simulated in both e-glass and carbon fibre. On this first approach, 18-layer laminates were used because the number of layers is not critical for the determination of the resonance frequency of the plies and the simulation of laminates with 42-49 layers increased needlessly the calculation time. The resonance frequencies of a 0.6 mm carbon-fibre ply and a 0.44 mm glass-fibre ply can be determined from the reflection-coefficient frequency spectrum of those laminates (see Figure 6).

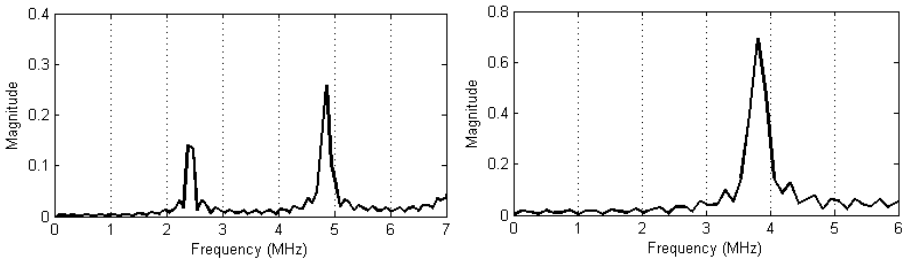

Figure 6: Reflection coefficient of an 18 layers carbon fibre laminate with a 0.6 mm ply spacing (left) and of an 18 layers e-glass fibre laminate with a 0.44 mm ply spacing (right).

The model shows that, for the carbon-fibre composite the fundamental resonance frequency, $F_{R1,}$ is 2.3MHz and the second-harmonic resonance, $F_{R2,}$ is 4.7MHz for a 0.6 mm ply spacing. For the glass-fibre composite, the fundamental resonance frequency was 3.8 MHz (F_{R1}) for a 0.44 mm ply spacing.

Additionally, the fundamental resonance frequency is a function of the ply thickness which changes considerably inside a wrinkle and also varies within the wrinkle region. The ply spacing decreases above the wrinkle where the layers are compacting causing an increase in the resonance frequency; and increases where the layers are expanding, causing a decrease in the resonance frequency. As an example, in the carbon-fibre laminate, a 3 mm amplitude wrinkle causes the ply thickness to decrease from 0.6 mm down to 0.43 mm at the point of highest amplitude of the wrinkle with an associated increase in the resonance frequency from 2.3 MHz up to 3.0 MHz. For this reason, the ideal probe needed to have a bandwidth that covers the range of resonance frequencies within the wrinkle.

In accordance with these first simulation results, two frequencies were considered for the experiments. On one hand, a 2.25 MHz broad-band probe with a 2.25 MHz pulse-echo bandwidth centred on the fundamental resonance of the unwrinkled carbon plies whilst including the glass-fibre ply-resonance frequency of 3.8 MHz. On the other hand, a 5 MHz narrow-band probe with a 2.5 MHz pulse-echo bandwidth centred on the fundamental glass-plies resonance that also enhances the reflection of the carbon plies at their second-harmonic frequency. In order to check the suitability of the considered probes, a 36 carbon-ply laminate (carbon-fibre plies of thickness 0.59 mm with 0.01 mm resin layers) with a 3 mm amplitude wrinkle in the middle was simulated. This laminate was used because the study samples are mainly carbon fibre, to see if the selected probes are capable to cover the thickness changes within the wrinkle but without considering yet the change of material. The simulated responses are shown in Figure 7 for both probe options.

As expected, the instantaneous phase increases by 2π radians for each ply traversed in the bulk of the material that is excited by the fundamental ply resonance and by 4π radians with an input-pulse that corresponds to the second harmonic[19]. This makes interpretation considerably easier for the 2.25 MHz probe, which excites the fundamental ply resonance of the non-wrinkle area and the whole range of ply thicknesses of the wrinkle are within the bandwidth of the probe. By contrast, the second harmonic of the plies is excited by the 5 MHz probe except in the zone of the wrinkle where the plies become thinner. Also, at 5 MHz, interpretation is more difficult because a single layer corresponds to 2 phase cycles in the non-wrinkle area. Also because the fundamental resonance frequency of the plies in the zone above the wrinkle increases until it dominates over the second harmonic and the phase only increases by 2π radians per ply so, in that area, a single layer corresponds to 1 phase cycle. The

simulated responses show that the wrinkle is tracked by both probe options in both amplitude and phase. Note that the amplitude peaks are always at the resin layers between plies, independent of frequency of probe. The amplitude response in the squashed-ply region above the wrinkle is different for the two probes. In this region the plies have approximately halved in thickness, pushing the fundamental resonance to about 5 MHz and the minimum spectral response to 2.5 MHz; this is an anti-resonance that is always at half the fundamental resonance. Thus, the 5 MHz probe response is a maximum amplitude (fundamental resonance) whilst the 2.25 MHz probe response is a minimum amplitude (anti-resonance).

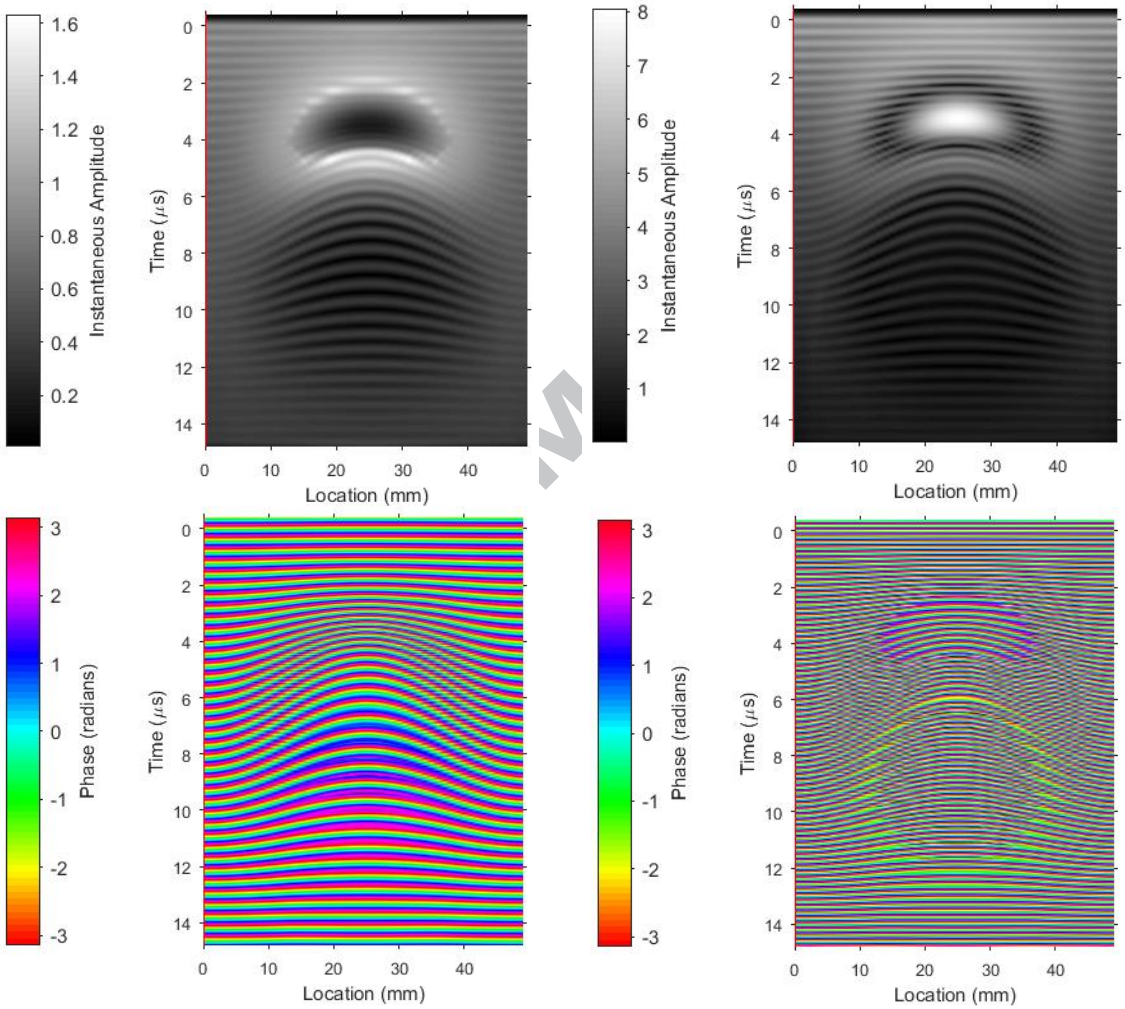

Figure 7. Simulated instantaneous amplitude (top) and phase (bottom) for 36 carbon-fibre plies of thickness 0.59 mm with 0.01 mm resin layers and a 3 mm amplitude wrinkle at the centre. 2.25 MHz centre frequency and 2.25 MHz bandwidth (left) and 5 MHz centre frequency and 2.5 MHz bandwidth (right).

Finally, mixed carbon/glass hybrid composites have been modelled (carbon-fibre plies of thickness 0.59 mm and 0.01 mm resin layers but with a 0.44 mm thick glass-fibre). The simulations with 2.25 MHz are shown in Figure 8. The glass-fibre woven plies are highly reflective and dominate the responses, making them much more complex. The higher reflection coefficient is at the glass-ply to resin-layer interface, due to the higher transverse stiffness of glass than carbon fibres, causing the resin-layer itself to be more reflective than the carbon-fibre equivalent. The reflection coefficient of the resin layer also depends on its thickness, which is approximately 0.01 mm in these samples. In

both amplitude and phase-response images, as well as the weaker reflections from carbon-fibre plies, the primary reflections from deeper glass plies are interfering with the multiple reflections from the earlier glass plies. The latter multiple reflections have erroneously exaggerated wrinkle angles, thus creating a very complicated interference pattern. The pattern in the real experiment may not be as complicated because the model assumes plane waves and infinite flat plies but of different spacings as the wrinkle is traversed. The experimental multiple reflections are expected to be at significantly lower amplitudes because the real laminate has angled plies in the wrinkle area.

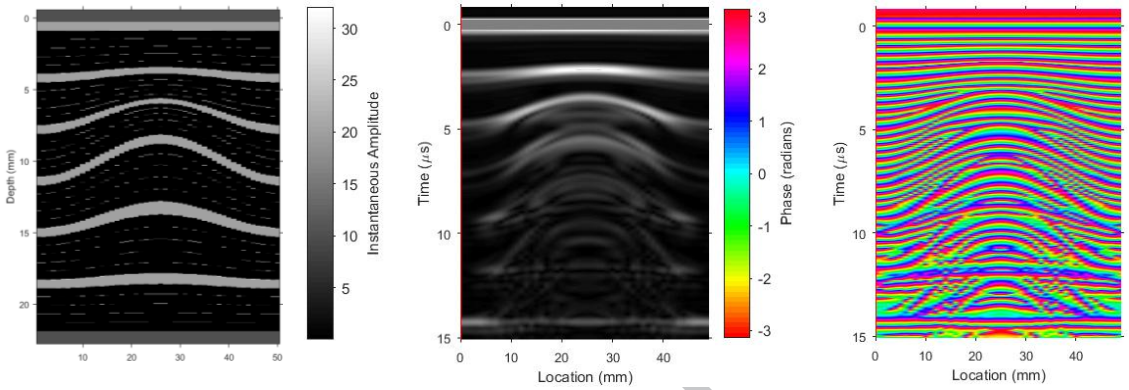

Figure 8. Simulated responses using a 2.25 MHz centre frequency and 2.25 MHz bandwidth for carbon-fibre plies of thickness 0.59 mm and 0.01 mm resin layers but with a 0.44 mm thick glass-fibre ply every 6th ply of a total 36 plies with a 3 mm wrinkle in the middle. Lay-up diagram (left), instantaneous amplitude (middle) and instantaneous phase (right).

In order to understand the superimposition of phases from multiple reflections in a wrinkled glass/carbon hybrid, it is proposed to first observe the instantaneous amplitude and phase response from a wrinkled component with much lower reflection coefficients and plies of several wavelengths thickness. An example would be the 6-MHz response of 1.5 mm carbon-fibre composite plies separated by 0.2-mm resin layers as in Figure 9. The amplitudes of any multiple reflections are very low but still sufficient to show up in the phase as there is no noise simulated in the modelled data. This effect should be taken into account when analyzing the actual inspections.

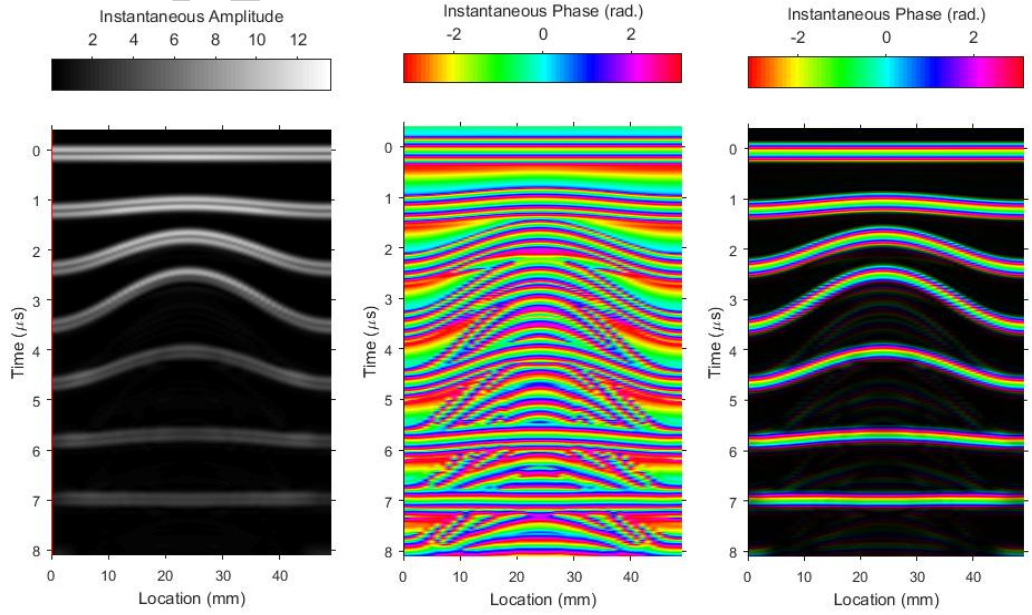

Figure 9. Simulated response from six 1.5 mm thick plies separated by 0.2 mm resin layers. (left) Instantaneous amplitude. (middle) Instantaneous phase. (right) Instantaneous phase in colour moderated by amplitude in brightness.

It should be noted that this one-dimensional analytical model does not simulate the effects of the highly anisotropic in-plane stiffness properties because it assumes normal incidence plane-wave ultrasound where only the transverse (to the fibres) compression modulus is required. It also ssumes flat in-plane plies and resin layers. A two- or three-dimensional model would be required to model the effects of this anisotropy and the geometrical complexity and the true geometrical distortions of the plies in order to predict the kind of imaging that is seen in the following experimental section of the paper. On-going work by the authors to implement and validate finite-element modelling in 2D and 3D will be reported in future publications.

5. Experimental ultrasonic testing results

5.1. Data-acquisition methods

Three inspections using different focusing methods were compared: full-matrix capture (FMC)[29] with reconstruction of B-scan slices using the total focusing method (TFM)[30], commercial phase-array technology and an immersion test with a raster-scanned single-element probe.

5.1.1 Full-matrix capture (FMC) with total-focusing method (TFM)

The FMC/TFM method is the current state of the art in imaging because every point reconstructed in the B-scan image uses a customised set of focal-law time delays to focus the responses from a large number of elements onto that point. There is an additional benefit in terms of signal-to-noise because the TFM algorithm combines multiple waveforms captured at different times, so the usual benefits of averaging are seen – a reduction in incoherent (temporal) noise that is inversely proportional to the square-root of the number of waveforms combined [29]. The FMC/TFM data acquisition was accomplished with 2.5 MHz and 5 MHz array probes connected to a Diagnostic Sonar 'FIToolbox' array controller. The Matlab-based BRAIN software developed at the University of Bristol [31] was used to reconstruct B-Scan slices of instantaneous amplitude and phase using the TFM software. Not all waveforms in the FMC array were used in the reconstruction algorithm because benefit has been shown[32] from limiting the angle of incidence to avoid side-lobes in the directional response. The angle limit in this case was 30° from normal incidence. All inspections were performed with the probe mounted directly on the surface of the sample, without a stand-off or wedge but coupled with gel.

However, FMC with TFM may not be needed to characterise the wrinkles. The more commercial Phase-array technology may also be adequate.

5.1.2 Commercial phased-array technology

Phased-array technology has been commercially available for non-destructive inspections for nearly twenty years and offers speed and imaging improvements over single-element probe scanning. Focal-law time delays are also used in this technology but they are applied in hardware to either the transmitted or received signals, or both. For this reason, only one focal depth can be used for each scan, although it would be possible to repeat the scan with a different focal depth. Some systems allow multiple focal depths to be used by consecutive acquisitions at each probe location. As a single

waveform acquisition is used, phased-array imaging does not have the same signal-to-noise benefits of the FMC/TFM method.

The wrinkled specimens were inspected using 2.25 MHz and 5 MHz phased-array probes and the OmniScan MX2 with a 16:64 Phased Array Unit – see Figure 10: Inspection setup. The instantaneous phase of the receiving wave is not provided by the OmniScan, so Matlab was used to process the received data. A coarse "instantaneous phase" was obtained, which just shows whether the real waveform (RF) is positive (black) or negative (white) – ie black for a phase ϕ of $-\pi/2 < \phi < \pi/2$ and white for a phase $\pi/2 < \phi < 3\pi/2$. With no stand-off, there was a significant dead zone at the top of the sample so the probes were used on a wedge stand-off. A 20-mm thick rexolite wedge was used with the 5 MHz probe and a 25-mm thick rexolite wedge was used with the 2.25 MHz probe.

Figure 10: Inspection setup

Phased-array probes (2.25L32-A5 probe with the SA5-OL-25MM wedge of thickness 25 mm and 5L64-NW1 probe with the SNW1-OL wedge of thickness 20 mm) were used for the experiments.

The back-surface echo is expected at 16.6 µs for specimen D and at 18.8 µs for specimens B and C; the compression-wave pulse-echo time-of-flight for the 25 mm-thick wedge (for the 2.25 MHz probe) is 21.5 µs and for the 20 mm-thick wedge (for the 5 MHz probe) is 17.2 µs. Therefore, at 5 MHz for specimens B and C, the multiple of the stand-off occurs before the back-surface echo. In addition, these wedges are solid and support shear-wave propagation, so mode-conversion between compression wave and shear wave can occur at the boundaries. This can cause a 'ghost' image of the front surface at approximately half of the wedge time of flight after the front-surface signal, due to either the outward or return signal being a shear wave.

5.1.3 Single-element immersion scanning with a spherically focused probe

Traditionally, composites are inspected after manufacture using single-element ultrasonic probes, which may be planar or focused and used in through-transmission or pulse-echo modes. In general, the intention is to measure the full-thickness ultrasonic attenuation and to detect any defects that reflect ultrasound. For characterising wrinkles, a focused probe with a focal depth set at the mid-plane of the material has been shown to be optimal[17]. Whilst the phased-array and FMC/TFM methods using linear arrays were only cylindrically focusing (in one plane), the single-element probe has a spherical

focus and this may offer some advantages, although the anisotropy of the material may make this a disadvantage.

The wrinkled specimens were finally inspected using an Ultrasonic Sciences Ltd full-waveform capture immersion scanning tank at the University of Bristol. The two immersion probes used for the experiments had spherically shaped focusing elements instead of planar elements. The characteristics of the probes used are summarised at Table 3.

Table 3: Characteristics of the immersion probes.

Frequency (f)	2.25 MHz	5 MHz
Element size (D)	9.525 mm	12.7 mm
Focal Length in water (F)	25.4 mm	38.1 mm
Maximum focal length in composite	12 mm	19 mm
Near Field Distance in water (N)	34.48 mm	136.22 mm
Normalized Focal Length (Sf)	0.74	0.28
Focal zone (Fz)	27.35 mm	18.70 mm
Beam Diameter (BD)	1.80 mm	0.91 mm

In an immersion test the ultrasonic beam propagates in two different media: water and the material (carbon and glass fibre). When the beam is generated in one medium and then coupled into another, the focal depth and the whole beam shape change. The new focal depth is calculated using the ratio of the acoustic velocities of the two media to adjust the portion of the beam in the second medium[33]. For the best imaging, the inspection requires that the distance between the probe and the sample is adjusted such that the ultrasonic beam is focused at the chosen depth inside the sample (usually the mid-plane). The distance between the probe and the front surface of the sample, the water path, was calculated using equation (3).

$$Water\ Path = F - x * \frac{c_{material}}{c_{water}} \qquad (3)$$

where c_{water} and $c_{material}$ are the sound velocities in water and the material respectively, F is the focal length of the probe in water and *x* is the distance between the front wall of the sample and the focal plane of the beam – ideally at the mid-plane of the sample. However, it was not possible to focus the 2.25 MHz probe at the mid-plane because the samples were too thick (see Table 1), so a depth of 5 mm was used.

5.2. Qualitative comparison of ply-tracking ability

B-scan cross-sectional images are shown in Figures 11 to 14 for all the specimens, data-acquisition techniques and frequencies used. They have been scaled in depth as well as possible for these figures to allow comparison but the horizontal scaling is arbitrary.

As expected from the analytical-model simulations, the results from the 2.5 MHz probe were easier to interpret. At 5 MHz, the instantaneous phase increases by 4π radians for each ply traversed in the bulk of the material that is excited by the second harmonic. Also, increasing the frequency decreased the penetration of the signal in the material causing only half the specimens to appear clearly represented in the images. In samples B and C, the glass-fibre layers have a dampening effect that prevents strong back-wall

echoes to be obtained. When inspecting those samples the use of the 2.25 MHz probe with a wide bandwidth seems a simple solution.

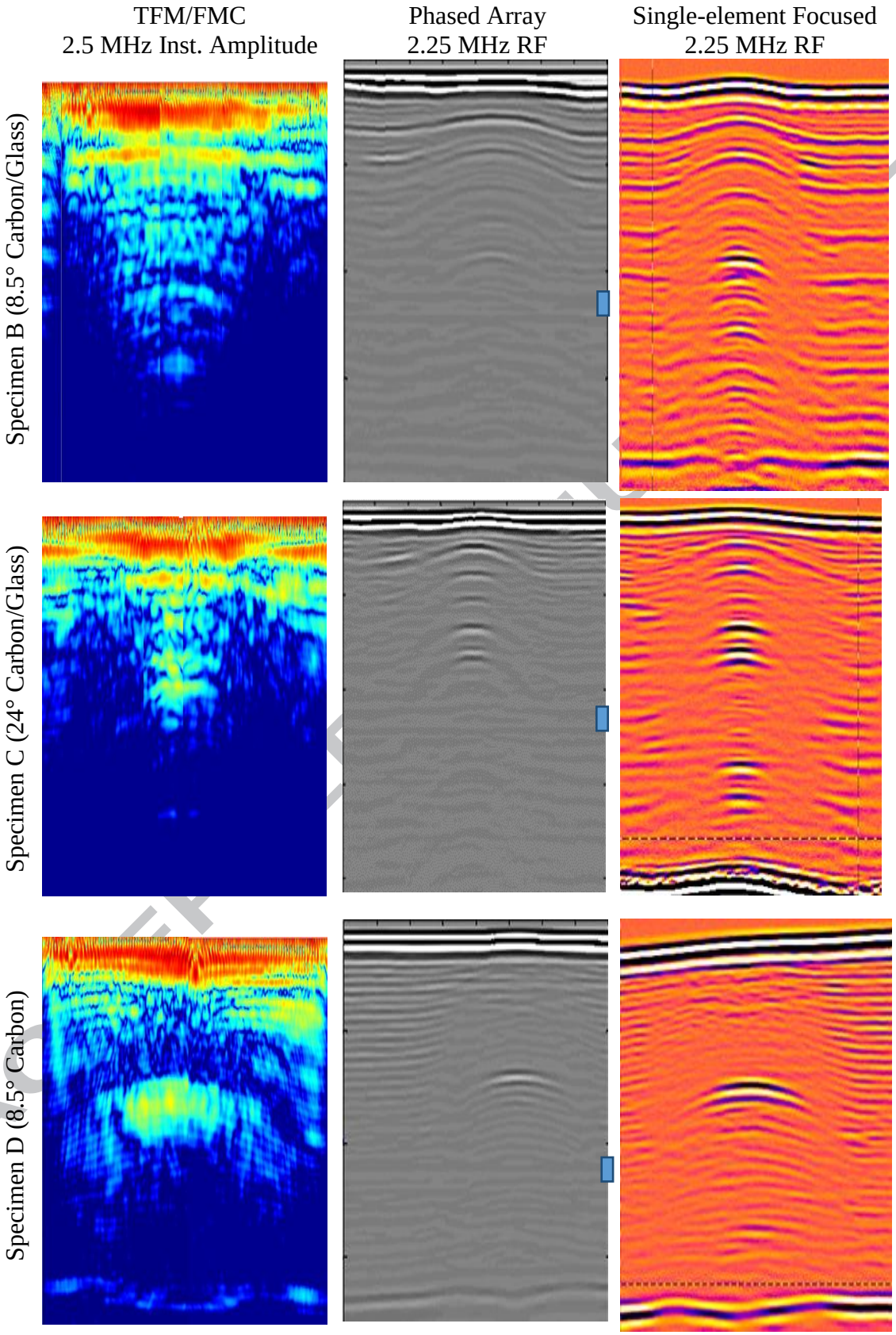

Figure 11. B-scan cross-sectional slices through the 2.25 MHz Amplitude / RF data for each specimen and data-acquisition technique. The blue rectangles indicate the depth of the artefact from the mixed-mode response of the phased-array stand-off.

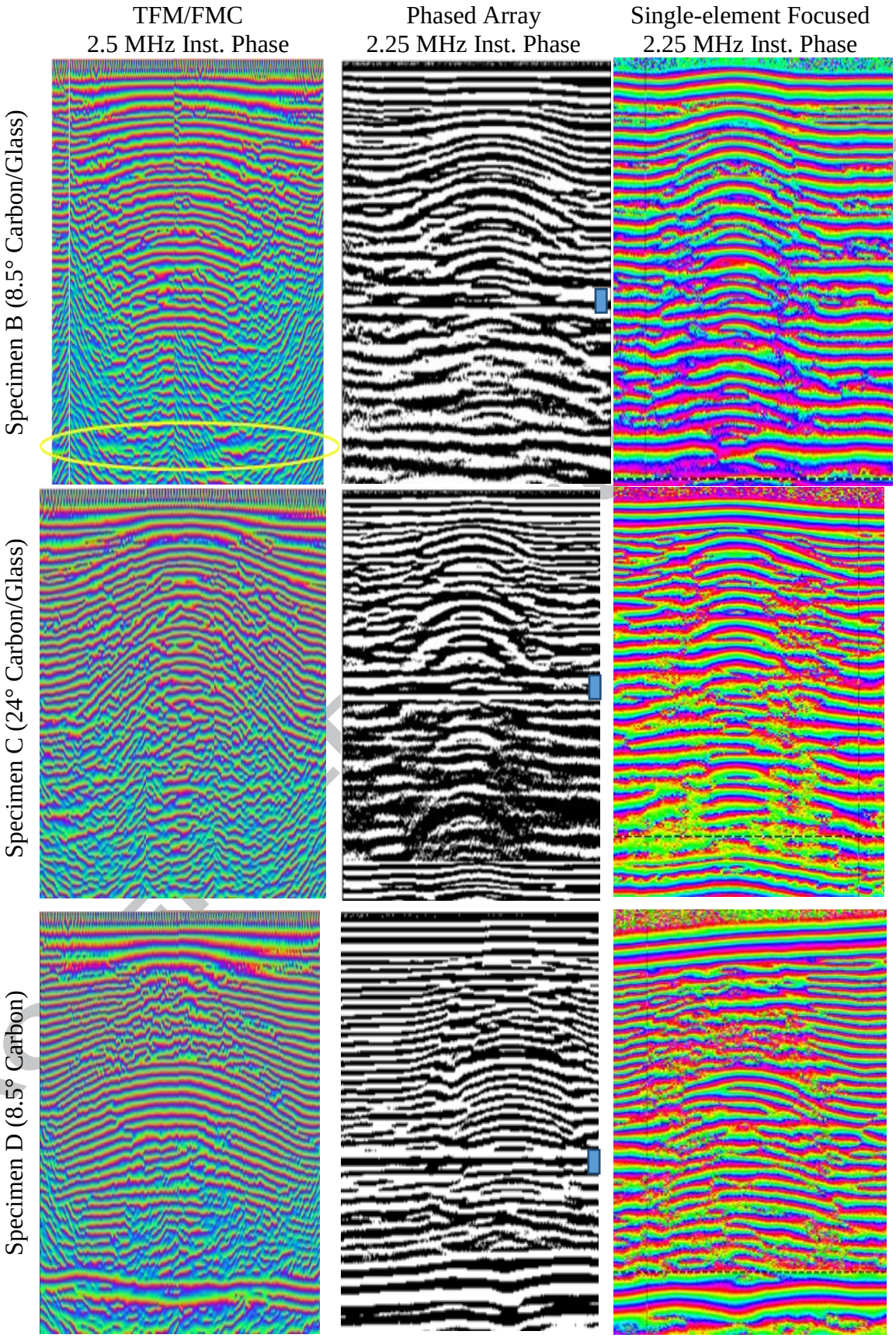

Figure 12. B-scan cross-sectional slices through the 2.25 MHz instantaneous-phase data for each specimen and data-acquisition technique. Note the yellow ellipse highlights the back-surface echo. The blue rectangles indicate the depth of the artefact from the mixed-mode response of the phased-array stand-off.

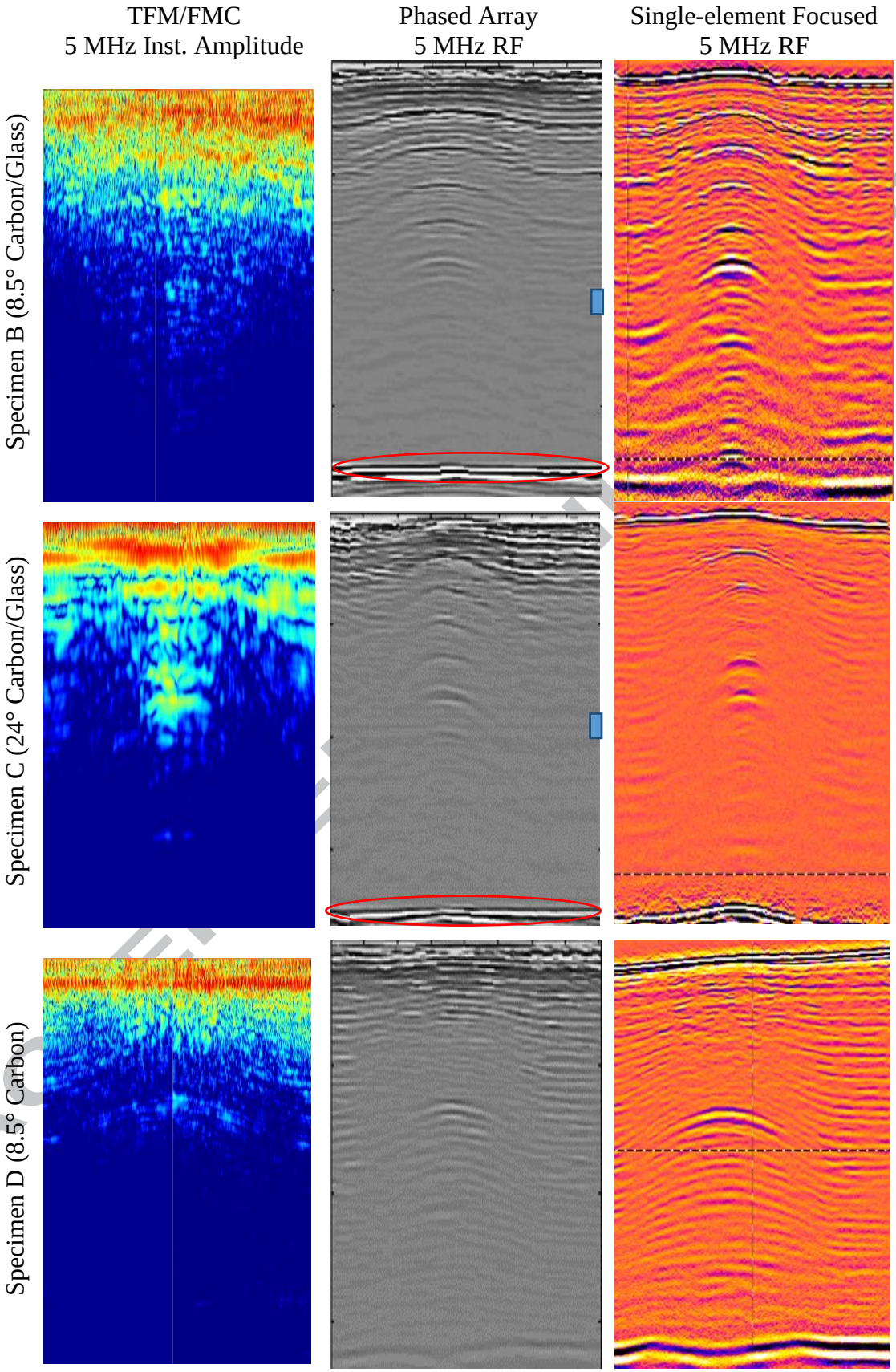

Figure 13. B-scan cross-sectional slices through the 5 MHz Amplitude / RF data for each specimen and data-acquisition technique. Note the red ellipses highlight the multiple echo from the stand-off. The blue rectangles indicate the depth of the artefact from the mixed-mode response of the phased-array stand-off.

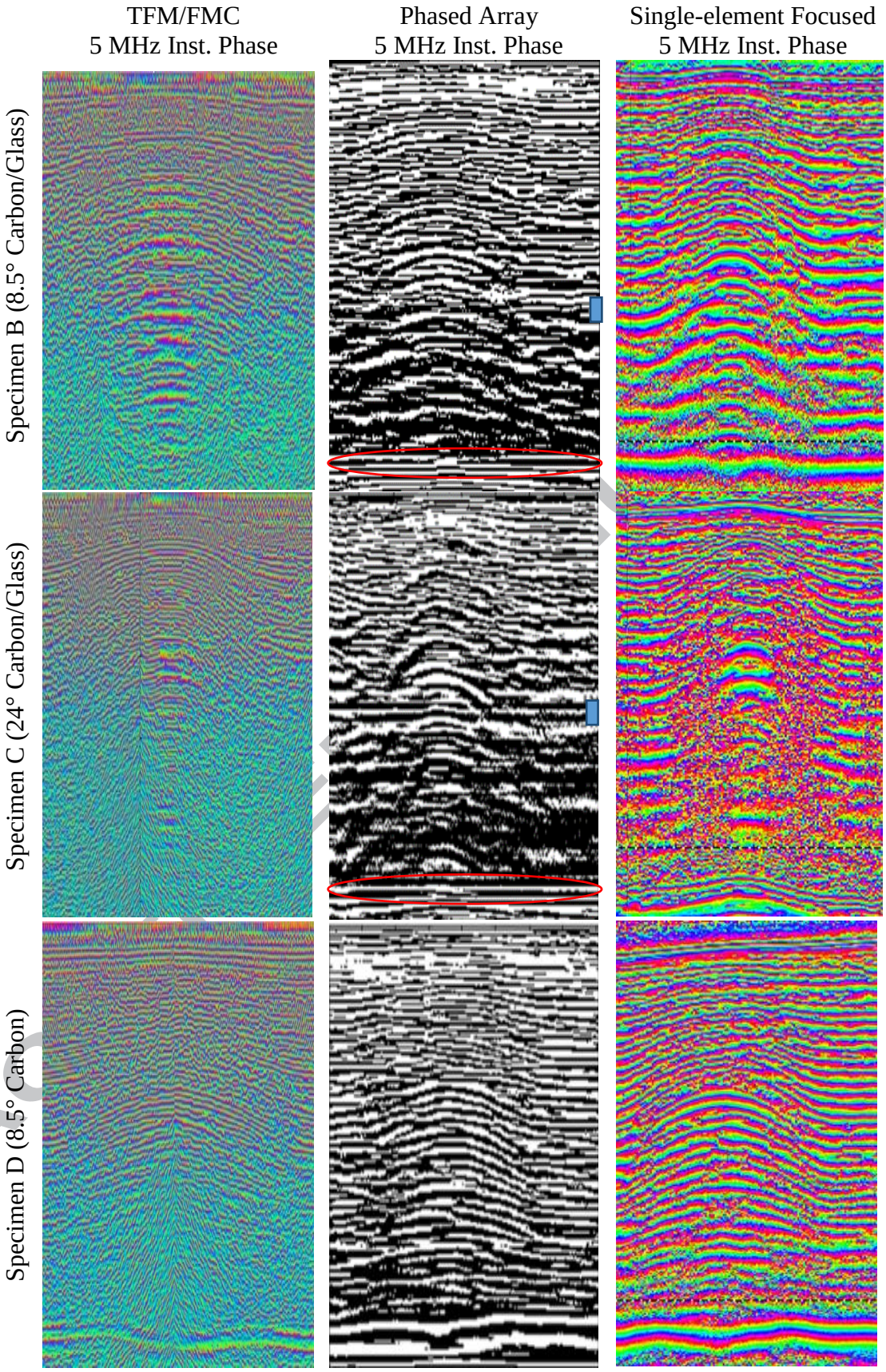

Figure 14. B-scan cross-sectional slices through the 5 MHz instantaneous-phase data for each specimen and data-acquisition technique. Note the red ellipses highlight the multiple echo from the stand-off and blue rectangles indicate the depth of the artefact from the mixed-mode response of the phased-array stand-off.

Artefacts

Before analysing the images, it is important to understand two sources of artefacts, both affecting just the phased-array images. The phased-array technique used solid stand-off wedges. The one for the 5 MHz probe was not quite thick enough for specimens B and C, so the multiple of the stand-off appears at around the same time-of-flight as the back surface echo in those images. These are shown encircled by a red ellipse in the figures. In addition, the hybrid compression-shear mode reflection from the front surface can be seen superimposed on both the amplitude and phase 2.25-MHz images – just beyond mid-way between the front and back surfaces. These are marked with a blue rectangle on the right-hand side in the figures.

Back surface

A back-surface echo is visible with FMC/TFM on Specimen D, in both phase and amplitude at 2.5 MHz, less strongly at 5 MHz but not at all for either of the other samples at either frequency, except a trace in the 2.5 MHz phase image for Specimen B (circled in yellow). This is presumed to be because Specimen D, containing only carbon composite, is less attenuative. The phased-array results are similar in that the back surface of Specimen D gives a stronger reflection than the other two specimens. The single-element immersion method shows strong back-surface echoes for all specimens and both frequencies, in amplitude and phase.

Ply imaging in flat regions

At the right and left edges of each image, the specimen has relatively flat, evenly spaced plies. In this region, all the techniques produced both amplitude and phase images that are relatively well locked to the plies of Specimen D, as predicted by the analytical model in Figure 8. However, the interference effects due to the glass plies in Specimens B and C are evident even in the flat-ply edge regions in the phase images, whilst the amplitude and RF images clearly show the stronger glass-fibre ply reflections, as predicted by the model in Figure 9.

Wrinkling

The imaging of wrinkles broadly agrees with the analytical-model simulations illustrated in Figures 8 and 9. For Specimens B and C the instantaneous amplitude is dominated by the glass-fibre plies every 6^{th} ply and the instantaneous phase contains a complex mix of carbon-fibre ply reflections superimposed on the strong glass-fibre ply reflections and their multiple reflections which have erroneously exaggerated wrinkle angles compared with the true wrinkling of the deeper plies themselves. For Specimen D, with no internal glass-fibre plies, the response is dominated by the uniform reflections of the resin layers between carbon-fibre plies. This explains why individual plies are imaged better than for Specimens B and C. However, the wrinkle-formation method appears to have left a very thick resin-rich layer in the middle of the specimen at the peak of the wrinkle, caused by bridging where the second half of the specimen was laid-up into the wrinkle formed by the tool in the first half of the specimen. This thick resin layer is predicted by the analytical model to cause an increased reflection coefficient, as explained above (reflection coefficient is approximately proportional to

the resin-layer thickness), and does indeed give an increased amplitude at this depth in the experimental amplitude and RF images using all three techniques.

Some wrinkling is just apparent in the FMC/TFM instantaneous-amplitude images but it is clearer in the RF images from the other two techniques, probably because the RF waveform contains phase information and the wrinkling is much more obvious in the instantaneous-phase images, as expected from the simulations in Figures 8 and 9.

In the wrinkle zone, when the thickness of the layers decreases significantly, it causes an increase in the resonance frequency to approximately 5 MHz preventing the tracking of every ply. This is most serious for Specimen D imaged at the lower frequency (2.25/2.5 MHz) where the phase imaging in the thin-ply region above the wrinkle is very poor (Figure 12). The bandwidth of the 2.25 MHz probes is insufficient for imaging the thin plies caused by the amplitude of the wrinkle in Specimen D and the probe centre frequency is at an anti-resonance, as discussed in the above modelling section. The 5 MHz images are significantly better because the fundamental resonance of the thin wrinkled plies as close to the second harmonic of the flat plies. For Specimens B and C, the thin-ply problem is dwarfed by the interference patterns produced by the glass-fibre plies, which dominate the response, allowing the wrinkles to be imaged and the plies tracked at both frequencies.

Specimen C had a much higher maximum wrinkle angle (24°) than specimens B and D (8.5°) and only the FMC/TFM method was able to image this steep angle well enough to measure it, and with only a 10% underestimate.

5.3. Quantitative wrinkle analysis

The wrinkle metrics were measured with an electronic rule and protractor on the B-Scan slices of instantaneous phase, as shown in Figure 1, which should be used to interpret the parameters.

It is important to note that no correction was applied to the wrinkle parameters to allow for the effect of changes in fibre volume fraction (FVF) on sound velocity. Inside a wrinkle, the FVF varies considerably, and this effect could distort the measurement of the amplitude, angle and "severity" [25]. This effect could be analysed in future work.

As expected from the analytical-model simulations, because sample D is all carbon composite, it was possible to measure all the proposed wrinkle parameters. However, specimen D was the only one that could be measured with the 5 MHz FMC/TFM or phased-array techniques. For Specimens B and C, the ply-interface lines are not clear at 5 MHz and are difficult to follow. For that reason, the wrinkle maximum height (H) and the angle θ were not measurable.

Table 4 summarise the results obtained and Figure 1 should be used to interpret the parameters.

Table 4: Comparison between the actual parameters of the wrinkles and those obtained from the convex side of the specimens by each of the three inspections.

Specimen and wrinkle parameters.		**Actual**	FMC/TFM		Phased Array		Single-element focused	
			2.5 MHz	5 MHz	2.25 MHz	5 MHz	2.25 MHz	5 MHz
B	H (mm)	**3**	3.6		3.15		3.1	
	L (mm)	53	47		63		55	
	A/L	**0.030**	0.038		0.025		0.028	
	θ	**8.5º**	9º		8.2º		7.5º	
C	H (mm)	**6**	6.5		4.1		4.0	
	L (mm)	**37**	43		41		50	
	A/L	**0.090**	0.075		0.050		0.040	
	θ	**24º**	22º		13º		14º	
D	H (mm)	**3**	3.2	3.5	2.6	2.1	2.9	2.9
	L (mm)	**53**	49	44	52	53	48	50
	A/L	**0.030**	0.033	0.040	0.025	0.020	0.030	0.029
	θ	**8.5º**	8.5º	10º	7.6º	6.7º	7.6º	7.4º

As the maximum wrinkle angle, θ, has been shown to be the key metric for determining the compression strength of a wrinkled composite[7], this should be the parameter that is used to compare the quantitative capabilities of the three experimental methods. As can be seen in Figure 15, the single-element and phased-array methods both underestimated the maximum wrinkle angle for all specimens but particularly for Specimen C, where the underestimate was about 50%. The FMC/TFM method had an estimated error in maximum wrinkle angle of approximately ±10%.

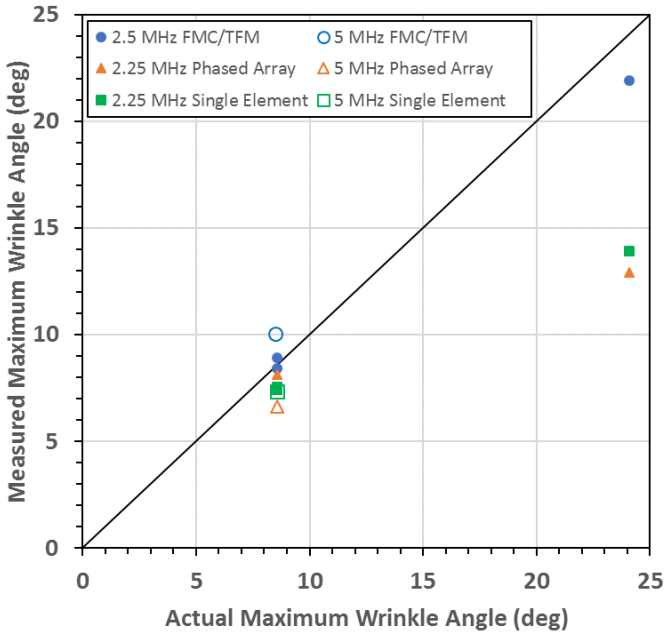

Figure 15. Graph showing a comparison of the measured and actual maximum wrinkle angles for the three methods and for 2.25 MHz (solid symbols) and 5 MHz (open symbols). The line represents where the measured angle equals the actual angle.

One of the major difficulties encountered in defining the wrinkle accurately was to follow in the image the line of maximum amplitude of the wrinkle. In many images, the area of the part where the maximum wrinkle angle is reached does not present a clear image.

The FMC/TFM allows the characterisation of the wrinkles with a reasonable precision using the instantaneous phase of the received signal and the resonant frequency as the appropriate inspection frequency.

With Phased-array technology, it was not possible to measure the wrinkle from the 5 MHz inspections because there are too many interferences and the stand-off/wedge mixed-mode front-surface echo appears across the maximum-wrinkle ply-interface line.

With single-element immersion scanning, the RF scans where used to measure samples B and C whereas the instantaneous phase of the receive signal was used to measure sample D, but only from the 2.25 MHz inspections. For the 5 MHz inspections, the ply-interface lines are not clear on any of the images.

The high relative errors in the measurements of the wrinkle of part C with the 2.25MHz probe suggests that one of the interference echoes that were predicted in the simulations has been measured erroneously for phased-array technology. This highlights the difficulty in discerning the main echoes in such complex patterns.

5.4. Comparison of results

The clear benefit demonstrated for the FMC/TFM method over both phased-array and single-element focused methods can be explained by the ability of the TFM method to focus the reconstructed ultrasonic beam on every point in the B-scan individually. This appears to improve the imaging of instantaneous phase, which is the parameter that is most sensitive to the wrinkle angle. However, the TFM reconstruction used in the above analysis assumed isotropic stiffness properties and therefore an ultrasonic velocity that is independent of the propagation direction in the material. It is clear that each waveform used to reconstruct the TFM image will have travelled in a different direction in the material and the material is actually anisotropic. Li et al.[32] have shown that an improvement to the TFM imaging is possible if an angle-dependent velocity is used in the TFM algorithm and this is the subject of the following section.

6. Adapted-TFM to account for anisotropic velocities

A recent study [32] has shown that a modification of the TFM reconstruction to account for the directional dependence of ultrasonic velocity improved the imaging of side-drilled holes in composite materials but did not optimise the method for imaging the composite plies, which is required for improving the wrinkle imaging. In addition, limiting the maximum incident angle of propagation has been shown to improve the Signal-to-Noise Ratio (SNR) of a defect [32]; this is due to a combination of the limited directional response of the array elements and the increase in mode conversion to transverse modes with increased angle. This section demonstrates the potential for a modified-TFM algorithm with angle-dependent velocity and a limited range incident angles to characterise wrinkles in the specimens studied. The TFM signal processing

was carried out using Brain (BRistol Array INspection) post-processing software [34]. To account for the angle-dependent velocity, the method first assumes that the material is homogeneous but anisotropic, to allow the same angle-dependence to be used at all locations. To determine the angle dependence, an experimental approach was used, based on the Back-wall Reflection Method (BRM) as described in Ref. [32, 35]. This is a quick and pragmatic method but requires the component to be flat with parallel front and back surfaces. A known non-wrinkled and defect-free region of the specimen is required to apply this method. A set of measured group velocities are then obtained for a range of propagation angles and incorporated into the TFM algorithm using a third-order polynomial fit to these points. Figure 16 shows the group velocity results as a function of propagation angle obtained for each specimen using 2.5 MHz and 5 MHz probes. As can be seen, the cubic fitting matches the velocity measurements well. Normally the upper angle limit that the BRM can cover depends on the transducer element pitch and specimen thickness. This highest angle is observed to be around 60 degrees for specimen C at 5 MHz (Fig.16e). However, values for higher angles can be calculated by using the Through-Transmission Method (TTM) [29]. The group velocities range between 3000 m/s to 7750 m/s, suggesting a high anisotropy of the specimens, as expected for carbon-fibre composite.

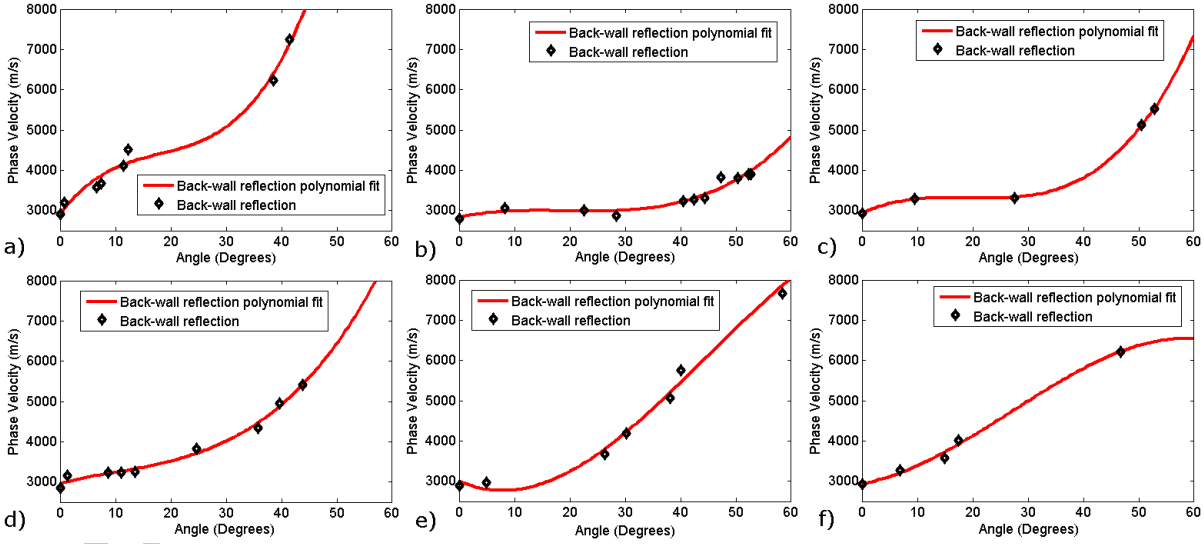

Figure 16: Measured phase velocities profile obtained using Back-wall Reflection Method (BRM) showing a third-order polynomial fit to the data. a) Specimen B at 2.5 MHz; b) Specimen C at 2.5 MHz; c) Specimen D at 2.5 MHz; d) Specimen B at 5 MHz; e) Specimen C at 5 MHz; f) Specimen D at 5 MHz;

A study to determine the optimised maximum propagation angle θ_{max} was carried out to reconstruct the FMC data set. For this, the signal-to-noise ratio (SNR) used in Ref. [32] is not appropriate because their 'noise' included the very reflections from inter-ply resin-layers that are required for the current study. So, for this study, noise is measured as the standard deviation in the instantaneous amplitude response from a non-wrinkled region. Thus, the SNR of the plies in the wrinkled region was calculated for the TFM results as

$$SNR\ (dB) = 20\ log_{10}\frac{I_{max}}{\sigma} \qquad (4)$$

where I_{max} is the maximum instantaneous amplitude in the reconstructed B-scan image for a specific wrinkle (for Specimen B this will be at a glass-fibre ply) and σ is the standard deviation of the noise from a rectangular region near to the selected wrinkle but in a region of roughly constant amplitude. Figure 17 depicts the SNR of specimen B for 2.5 MHz as a function of the maximum propagation angle θ_{max}. One can observe that the maximum of SNR is obtained for a maximum propagation angle of 35 degrees. This observation is also consistent with the work by Li et al. [32], which proved that the use of the optimum angle would help to improve the detectability of some reflectors or defects in the composite material.

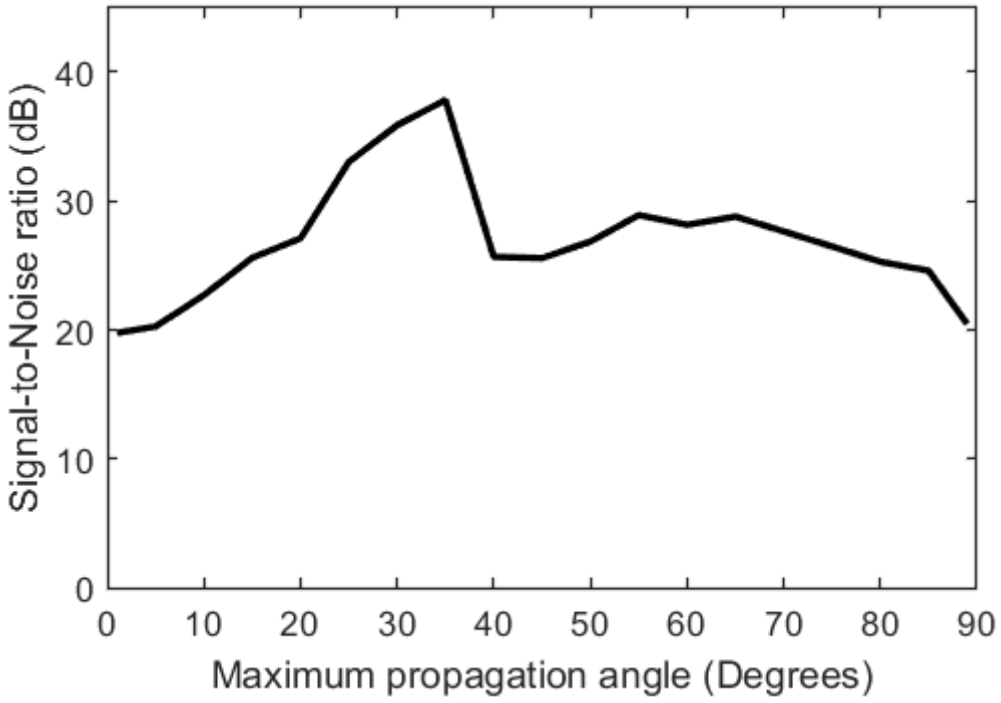

Figure 17: Signal-to-Noise ratio for a wrinkle located half way through specimen B as a function of the maximum propagation angle for TFM results.

The maximum propagation angle of 35 degrees is then used to reconstruct the TFM images for the specimens studied using the adapted-TFM algorithm. Figure 18 shows the TFM instantaneous-phase image obtained for specimen B at 2.5 MHz with a maximum propagation angle of 35 degrees. In this figure, the normal TFM, adapted-TFM and analytical model images are compared. It is observed that characterisation of the wrinkles is better for the adapted-TFM, particularly at the higher ply angles, than for the previous results obtained with the normal TFM algorithm. In particular, the analytical-model predicted near-surface interference response from the glass and carbon plies has been faithfully reproduced in the adapted-TFM image but is difficult to see in the normal TFM image. Deeper in the structure, the interference of the glass-fibre plies seems to diminish relative to the modelled prediction, probably due to the two-dimensional nature of the experimental TFM method, which responds differently to angled plies in a focused field, compared with the one-dimensional analytical model, which assumes infinite in-plane interfaces and plane-wave ultrasound. The results demonstrate the potential benefit of using an angle-dependent velocity in the TFM method to image the crucial maximum-angle section of a wrinkle. The measured

maximum wrinkle angle is unaffected in this case because the improvement in imaging was not required for this particular measurement, but is useful for proving that the correct location of maximum angle has been identified.

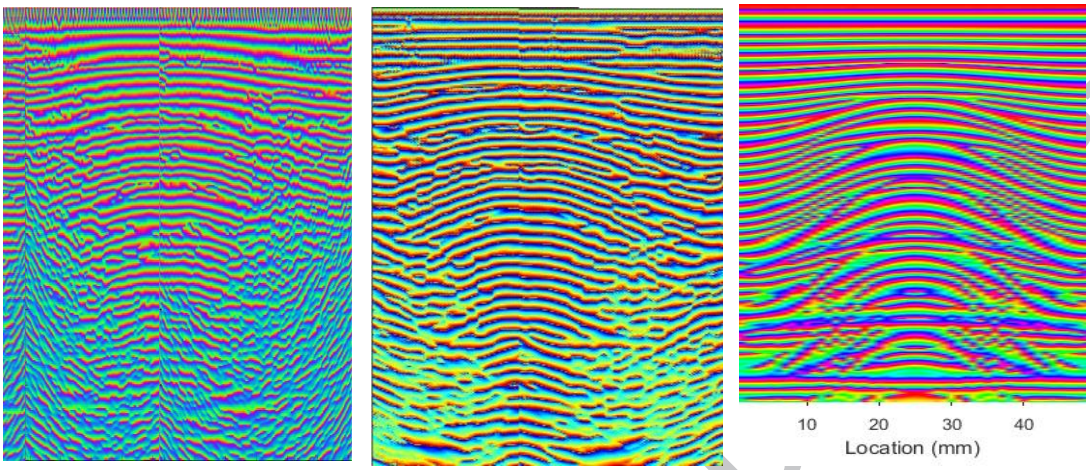

Figure 18: Comparison of the normal (isotropic) TFM algorithm (left) with the adapted-TFM instantaneous-phase result (centre) for Specimen B for 2.5 MHz with a maximum propagation angle of 35 degrees. These are compared with the analytical model results for Specimen B (right) from Figure 8.

7. Conclusions

This paper compares three different ultrasound techniques that can be used to detect and characterise wrinkles in thick-section glass-carbon hybrid laminates. The FMC/TFM method gave better results whilst phased-array technology and single-element immersion testing presented more challenges. This is explained by the superior focusing of TFM where every point in the B-scan image is made a focal point for reconstruction. To extend this further, an adapted-TFM algorithm was tested for the most complex sample – with a glass-fibre ply every sixth ply - and was compared with the standard TFM and the analytical model. There is a clear benefit in using the angle-dependent velocity correction within the adapted-TFM method, resulting in enhanced instantaneous-phase imaging of the whole wrinkle, particularly the steepest wrinkle angle and good agreement with the analytical-model results. The complex interferences in the experimental phase image diminish with depth whereas they increase with depth in the analytical-model phase image. This can be explained by the limitations of the one-dimensional, plane-wave, normal-incidence approximations of the analytical model and future work will include 2D and 3D finite-element modelling to prove this.

Using the optimum inspection frequency (the ply-resonance frequency) is essential to obtain images that are easy to interpret and use to measure wrinkle parameters. The instantaneous-phase images proved best for visualising plies in the wrinkle. A stand-off is required that is thick enough to put its multiple echo beyond the back-surface echo and a liquid stand-off is preferred to avoid the mixed-mode reflection of the front surface, which comes in the middle of the sample image.

Not all of the techniques allowed full characterisation of out-of-plane waviness on these specimens. All the techniques allowed the characterisation of a wrinkle in a UD carbon

sample with a reasonable accuracy. For hybrid glass-carbon laminates, the glass layers make the inspections more difficult, because of the high reflectivity of the glass layers and the occurrence of a complex interference pattern. Phased-array technology presented similar results to the immersion tests, but the experimental results still show significant errors, probably due to artefacts caused by the solid stand-off wedge used. The method that has been used to measure the wrinkles requires the presence in the image of a clear line that tracks the maximum wrinkle amplitude. It is expected that less demanding specimens would allow a better characterization of the defect regardless of the inspection method.

Acknowledgements: The authors in this research would like to acknowledge the support from "Consejo Social de la Universidad de Madrid" for the Fellowship granted to Ms Larrañaga Valsero for a Research Visit to the University of Bristol. The purchase of the Olympus NDT Data Access Library for the OmniScan has been supported by the project TRA2014-58263-C2-2-R funded by the National Research program of Spain. The authors would also like to thank Olympus and specially Mr. Andre Lamarre, for their support in making it possible for the authors to use the 2.25 MHz phase-array probe.

Author Contributions: Beatriz Larrañaga Valsero is the main author of this work. Antonio Fernandez Lopez and Alfredo Güemes have contributed as her advisors, firstly proposing the subject, reviewing the literature and obtained results. Robert A. Smith and Rostand B. Tayong have contributed as her advisors during her research visit to the University of Bristol, reviewing the literature and obtained results. Rostand B Tayong helped with the immersion scanning, FMC/TFM and the adapted-TFM with angle-dependent velocity correction, whilst Robert A. Smith modified his pre-existing analytical model to include hybrid composites with some glass plies in mainly carbon composite and to model the wrinkle geometries that were inserted in the components.

Conflicts of Interest: The authors declare no conflict of interest.

References

1. Sun, Shengpeng, et al., Review on wind power development in China: Current situation and improvement strategies to realize future development. Renewable and Sustainable Energy Reviews 45 (2015): 589–599.
2. H.M. Hsiao and I.M. Daniel, Effect of fiber waviness on stiffness and strength reduction of unidirectional composites under compressive loading, Composites Science and Technology, 56, (1996), 581-593.
3. George Marsh, The challenge of wind turbine blade repair, Renewable Energy Focus, Volume 12, Issue 4, July–August 2011, Pages 62-66
4. Paul Davidson and Anthony M. Waas, The effects of defects on the compressive response of thick carbon composites: An experimental and computational study, Composite Structures 176 (2017) 582–596
5. K. Potter, B. Khan, M. Wisnom, T. Bell and J. Stevens, Variability, fibre waviness and misalignment in the determination of the properties of composite materials and structures, Composites: Part A. 39 (2008) 1343-1354.

6. D.O. Adams and S.J. Bell, Compression Strength reductions in composite laminates due to multiple-layer waviness, Composites Science and Technology 53 (1995) 207-212.
7. Ningbo Xie, Robert A. Smith, Supratik Mukhopadhyay, Stephen R. Hallett, A numerical study on the influence of composite wrinkle defect geometry on compressive strength, Materials and Design 140 (2018) 7–20.
8. Tomo Takeda, Micromechanics model for three-dimensional effective elastic properties of composite laminates with ply wrinkles, Composite Structures 189 (2018) 419-427.
9. Ruizhen Yang, Yunze He, Hong Zhang, Progress and trends in nondestructive testing and evaluation for wind turbine composite blade, Renewable and Sustainable Energy Reviews 60 (2016) 1225–1250.
10. G Nikishkov, Y Nikishkov and A Makeev, Finite element mesh generation for composites with ply waviness based on X-ray computed tomography, Advances in Eng Software, Vol 58, pp 35-44, 2013.
11. R. A. Smith, L. J. Nelson, N. Xie, C. Fraij and S. R. Hallett, Progress in 3D characterisation and modelling of monolithic carbon-fibre composites, Insight, 57, 2015, pp. 131-139.
12. Mook G, Lange R, Koeser O. Non-destructive characterisation of carbon-fibre-reinforced plastics by means of eddy-currents. Compos Sci Technol 2001; 61:865–73.
13. K. Mizukami, Y. Mizutami, K. Kimura, A. Sato, A. Todoroki, Y. Suzuki, Detection of in-plane waviness in cross-ply CFRP laminates using layer selectable eddy current method, Composites: Part A. 82 (2016) 108-118.
14. K. Mizukami, Y. Mizutami, K. Kimura, A. Sato, A. Todoroki, Y. Suzuki, Visualization and size estimation of fiber waviness in multidirectional CFRP laminates using eddy current imaging, Composites: Part A. 90 (2016) 261-270.
15. R.A. Smith and B. Clarke, Ultrasonic C-scan determination of ply stacking sequence in carbon-fibre composites, Insight - Journal of the British Institute of NDT, Vol. 36, No. 10,1994, pp. 741-747.
16. D. Hsu, D. Fei and Z. Liu, Ultrasonically mapping the ply layup of composite laminates, Materials Evaluation, Vol 60 (9), 2002, pp 1099-1106.
17. Nelson, L.J., Smith, R.A., Mienczakowski, M., Ply-orientation measurements in composites using structure-tensor analysis of volumetric ultrasonic data, Composites: Part A, Vol 104, pp 108-119 (2018)
18. R. Smith, S. Hallett, P. Wilcox, L. Nelson, R. Tayong Boumda, N. Xie, and C. Fraij, Progress in non-destructive 3D characterization and modelling of aerospace composites, NDT of Composites II: Promoting Quality in Composite Inspection American Society of Nondestructive Testing (2015) pp. 38-44
19. R. A. Smith, L. J. Nelson, M. Mienczakowski, P. D. Wilcox, Ultrasonic analytic-signal responses from polymer-matrix composite laminates, IEEE Transactions on Ultrasonics, Ferroelectrics, and Frequency Control, , Vol. 65, Nº. 2, 2018, pp 231-243.

20. K. Subhash, The discrete Hilbert transform. *Proc. IEEE*, vol. 58, pp. 585–586, 1970.
21. B. Boashash, Estimating and Interpreting the Instantaneous Frequency of a Signal-Part I: Fundamentals, *Proc. IEEE*, vol. 80, no. 4, pp. 519-538, 1992
22. AENOR: Norma UNE-EN ISO 527-5:2010. [Internet]. 2010. Available online: http://www.aenor.es/aenor/normas/normas/fichanorma.asp?tipo=N&codigo=N0045182#.WgCNH4ZrzaI (accessed on 6 November 2017).
23. ASTM D695—15 Standard Test Method for Compressive Properties of Rigid Plastics [Internet]. Available online: https://www.astm.org/Standards/D695.htm (accessed on 6 November 2017).
24. AENOR: Norma UNE-EN ISO 14126:1999. Available online: http://www.aenor.es/aenor/normas/normas/fichanorma.asp?tipo=N&codigo=N0024654#.WluUL67iY7Y (accessed on 6 November 2017).
25. R. A. Smith, L. J. Nelson, M. J. Mienczakowski and P. D. Wilcox. Ultrasonic Tracking of Ply Drops in Composite Laminates. Proc. Review of Quantitative NDE, Minneapolis, July 2015, published in AIP Conference Proceedings 1706, 050006 (2016); doi: 10.1063/1.4940505, 2016.
26. R. A. Smith, Use of 3D ultrasound data sets to map the localised properties of fibre-reinforced composites, PhD Thesis, University of Nottingham, July 2010.
27. Z. Hashin, On elastic behaviour of fiber reinforced materials of arbitrary transverse phase geometry, J. Mech. Phys. Solids, vol. 13, pp. 119-134, 1965.
28. Z. Hashin, Analysis of properties of fiber composites with anisotropic constituents. J. Appl. Mech., vol. 46, pp. 546–550, 1979.
29. C. Holmes, B. W. Drinkwater and P. D. Wilcox, Post-processing of the full matrix of ultrasonic transmit-receive array data for non-destructive evaluation, NDT&E International 38, 2005, pp 701-711.
30. J. Zhang, B.W. Drinkwater, P.D. Wilcox, A. J. Hunter, Defect detection using ultrasonic arrays: The multi-mode total focusing method, NDT&E International 43 2010, pp 123-133.
31. http://www.bris.ac.uk/engineering/research/ndt/research/array-imaging/
32. C. Li, D. Pain, P.D. Wilcox, B.W. Drinkwater, Imaging composite material using ultrasonic arrays, NDT&E International 53 2013, pp 8-17.
33. Ginzel E. A. Near field and focusing considerations with wedges. 2009. Materials Research Institute, Waterloo, ON, Canada, Technical Report.
34. Source: https://sourceforge.net/projects/bristol-brain/
35. D. Yan, M. Sutcliffe, B. Wright, I. Cooper, Ultrasonic imaging of full matrix capture acquired data for carbon fibre-reinforced polymer, Insight – Non-Destructive Testing and Conditioning Monitoring 55(9) 2013, pp 477-481.